Computed Poststenotic Flow Instabilities Correlate Phenotypically With Vibrations Measured Using Laser Doppler Vibrometry: Perspectives for a Promising In Vivo Device for Early Detection of Moderate and Severe Carotid Stenosis

Viviana Mancini[1]
IBiTech-bioMMeda,
Ghent University,
Gent 9000, Belgium
e-mail: viviana.mancini@ugent.be

Aslak W. Bergersen[1]
Department of Computational Physiology,
Simula Research Laboratory,
Fornebu 1364, Norway

Kristian Valen-Sendstad
Department of Computational Physiology,
Simula Research Laboratory,
Fornebu 1364, Norway

Patrick Segers
IBiTech-bioMMeda,
Ghent University,
Gent 9000, Belgium

Early detection of asymptomatic carotid stenosis is crucial for treatment planning in the prevention of ischemic stroke. Auscultation, the current first-line screening methodology, comes with severe limitations that create urge for novel and robust techniques. Laser Doppler vibrometer (LDV) is a promising tool for inferring carotid stenosis by measuring stenosis-induced vibrations. The goal of the current study was to evaluate the feasibility of LDV for carotid stenosis detection. LDV measurements on a carotid phantom were used to validate our previously verified high-resolution computational fluid dynamics methodology, which was used to evaluate the impact of flowrate, flow split, and stenosis severity on the poststenotic intensity of flow instabilities (IFI). We evaluated sensitivity, specificity, and accuracy of using IFI for stenoses detection. Linear regression analyses showed that computationally derived pressure fluctuations correlated ($R^2 = 0.98$) with LDV measurements of stenosis-induced vibrations. The flowrate of stenosed vessels correlated ($R^2 = 0.90$) with the presence of poststenotic instabilities. Receiver operating characteristic analyses of power spectra revealed that the most relevant frequency bands for the detection of moderate (56–76%) and severe (86–96%) stenoses were 80–200 Hz and 0–40 Hz, respectively. Moderate stenosis was identified with sensitivity and specificity of 90%; values decreased to 70% for severe stenosis. The use of LDV as screening tool for asymptomatic stenosis can potentially provide improved accuracy of current screening methodologies for early detection. The applicability of this promising device for mass screening is currently being evaluated clinically. [DOI: 10.1115/1.4046586]

Keywords: asymptomatic carotid disease, auscultation, computational fluid dynamics (CFD), stenosis severity, laser Doppler vibrometer (LDV), intensity of flow instabilities (IFI)

1 Introduction

More than three million people died worldwide due to an ischemic stroke in 2017 [1], where the underlying disease was carotid stenosis in one of ten stroke patients [2]. Early detection could decrease mortality [3] and impact elective therapy [4]. However, the majority of carotid stenoses is asymptomatic and rarely detected. The most common clinical screening method for asymptomatic carotid stenosis is auscultation of the poststenotic turbulence-induced carotid bruit [5–7]. Carotid auscultation's specificity is approximately 80%, but sensitivity is operator-dependent and varies from 50% to 70% [8,9].

Poststenotic pressure fluctuations induce vibrations in the arterial wall, which propagate as mechanical waves to the skin, and manifests as vibrations or sound waves [10]. Extensive studies have been performed on the analysis of the downstream-stenosis turbulence [11,12]. Furthermore, the poststenotic flow instabilities are well known to be affected by stenosis degree, the volumetric flowrate in the common carotid artery, and the flow split between the internal carotid artery and external carotid artery [13,14]. However, to the best of our knowledge, no study systematically analyzed a complete combination of these factors potentially affecting the intensity of flow instabilities, varying over the pathophysiological range, or addressed the correlation between (the intensity of) stenosis-induced flow instabilities and skin vibrations.

Laser Doppler vibrometer (LDV) is a promising method for inferring carotid stenoses as a result of its high spatiotemporal resolution (10 nm, 10 μs) [15]. We recently performed an in vitro experiment [16] using a novel multibeam LDV [15] to measure the displacement of the surface of the gel embedding a compliant replicate of a patient-specific carotid bifurcation stenotic model. We found a significant correlation between flowrate and the wall displacement in the 0–200 Hz range. The experiment, intended as a proof-of-concept for showing that the LDV could be used for inferring the presence of asymptomatic carotid stenosis, was

[1]V. Mancini and A. W. Bergersen contributed equally to this work.

Manuscript received August 30, 2019; final manuscript received February 1, 2020; published online April 27, 2020. Assoc. Editor: Keefe B. Manning.

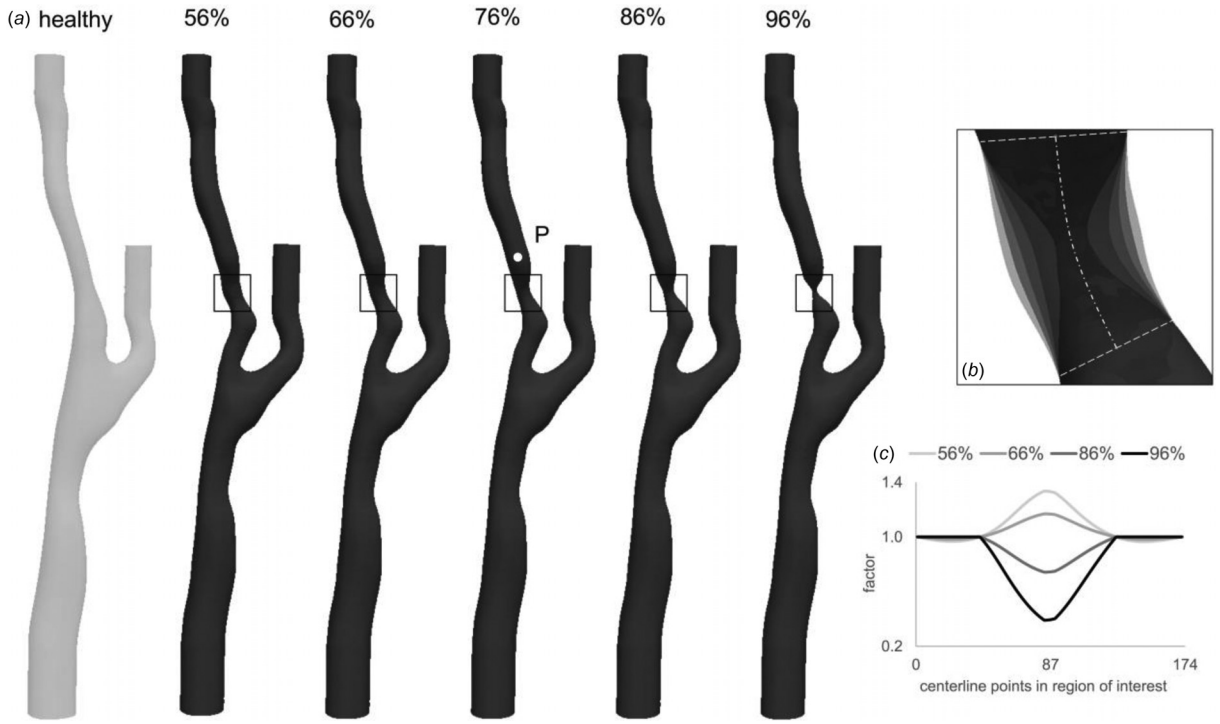

Fig. 1 (*a*) The healthy and 76% stenosis were obtained from computer tomography angiography images [19]. The remaining four degrees of stenosis were obtained by multiplying the cross-sectional area of the original stenotic geometry [20] within the region marked by the dashed lines reported in (*b*) with the *factor* reported in (*c*). Furthermore, in (*b*) the details of the stenosed geometries are shown as overlapped, and the centerline of the models is reported as a dotted–dashed line. The pressure field was probed at point P located 1D downstream of the stenosis on the centerline of the ICA.

limited to only one degree of stenosis. Computational fluid dynamics (CFD), on the other hand, has established itself as a key methodology to cheaply assess relevant fluid dynamical quantities [17], allowing for parametric studies that, in contrast, would be experimentally labor-intensive. Furthermore, we recently conducted a study to identify the sufficiently accurate numerical methodology to simulate downstream-stenosis flow instabilities [18].

The aim of this study was threefold: (i) to assess the validity of using CFD to mimic the physics of the phenomenon whereby flow instabilities induce high-frequency pressure oscillations that propagate to skin level, (ii) to analyze the parameter space of pathological and healthy models, in order to provide a correlation between flowrate, flow split, and stenosis severity and the intensity of poststenotic instabilities; (iii) to investigate the receiver operating characteristics (ROC) derived sensitivity, specificity, and accuracy of using LDV to infer the presence of a stenosis, by populating the correlation previously found in (ii) with a resolution and variability reflective of a population, therefore obtaining a fictitious clinical study.

As such, the presented study does not aim to provide a comprehensive understanding of the poststenotic flow field, but rather a proof-of-concept of the ability of the LDV to detect stenosis with physiologically plausible flow conditions in this specific carotid bifurcation geometry.

2 Methods

2.1 Computational Fluid Dynamical Model. We took advantage of the patient-specific geometry presented in Iannaccone et al. [19], which was a segmentation of a carotid bifurcation of a 75 y/o man with a 76% stenosis in the internal carotid artery (ICA). With a focus on assessing the impact of stenosis severity, we used the plausible prelesion lumen, segmented by Iannaccone et al. [19], as a healthy control. Furthermore, we obtained four additional degrees of stenosis, varying from moderate to extremely severe (56%, 66%, 86%, and 96%), by adapting the open-source tool *morphMan* [20] on the segmented 76% stenotic geometry (see Fig. 1(*a*)). Specifically, the cross-sectional area of the original model within the region of interest (Fig. 1(*b*)) was multiplied by a *factor* (Fig. 1(*c*)). Finally, the centerlines and the Voronoi diagram of the surfaces were used to obtain the four geometries. Please refer to Kjeldsberg et al. [20] for a more thorough description of the methodology.

The healthy and the five additional models, each with a different degree of stenosis, were meshed using VMTK [21] with four boundary layers and a local refinement in the stenosis area or, for the healthy geometry, where the stenosis developed. The spatial resolution, measured as averaged cell length (Δx_{mean}), was set to $\Delta x_{\text{mean}} = 1.92 \times 10^{-4}$ m (error $< 5\%$ with respect to Richardson's extrapolated solution [22]) accordingly to the spatial refinement study that was recently performed with a focus on the turbulent-like flow features on the same model [18], resulting in 32 tetrahedral cells across the stenosis area in the original 76% geometry.

Furthermore, we varied the volumetric flowrate (Q) imposed at the common carotid artery (CCA) and the flow split between ICA and external carotid artery based on the in vivo variability reported in three clinical studies [23–25]. A combination of all possible permutations between stenosis degree, Q_{CCA} and $Q_{\text{ICA}}/Q_{\text{CCA}}$ leads to 150 simulations, as a result of setting the mean-one and two standard deviations (SDs) for Q_{CCA} and $Q_{\text{ICA}}/Q_{\text{CCA}}$ for each of the six degrees of stenosis. Only a subgroup of the possible scenarios was run, in order to efficiently cover a wide range of physiological conditions. The simulations were organized into five categories. The first category consists of six simulations carried out on several degrees of stenosis with boundary conditions matching mean physiological values reported on a population level [23,24]. In the second and third category, we used the 76% stenosis model and changed the CCA flowrate and the ICA flow

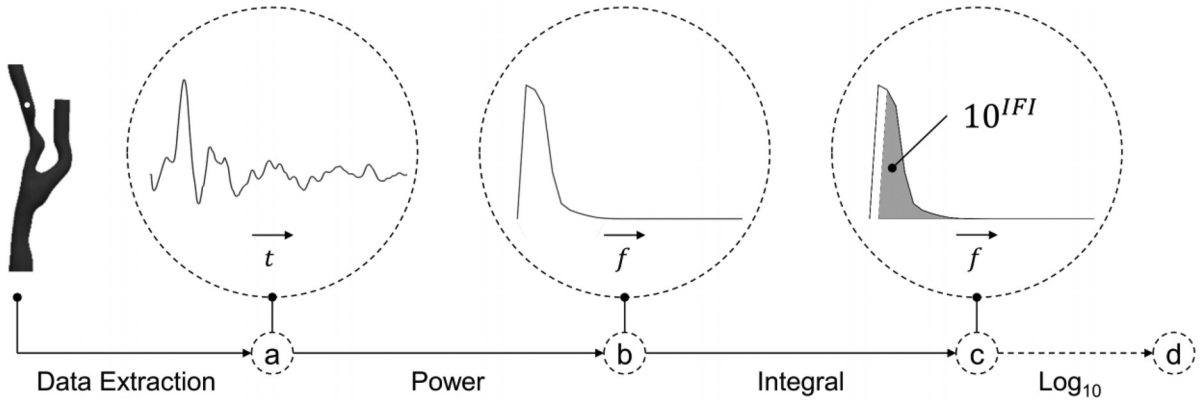

Fig. 2 Postprocessing workflow applied to both computational and experimental data

split, separately with ±1 and 2 SDs. The flow split of the healthy model was changed as −1 and 2 SDs in the fourth category. In the fifth category, we simultaneously varied a combination of multiple parameters, in order to populate the parameter space with permutations matching a Reynolds number between 300 and 380, in which we observed a phenotypical change in the flow field of intermediate results, resulting in five simulations. In total, encompassing all categories, we ran 21 simulations with Q_{CCA} varying from 145 to 529 ml/min and Q_{ICA}/Q_{CCA} from 11.9 to 70.8% (Table 1), reflecting the physiological range [26]. To contain the influence of the numerical setting on the solution, the flow split was imposed by setting its complementary value at the outlet of the external carotid artery, while a zero pressure boundary condition was set at the ICA outlet.

The walls of the model were assumed as rigid, as commonly used for the biomechanical analysis of healthy and stenotic carotid arteries [27]. Blood was modeled as a Newtonian fluid [28,29] with kinematic viscosity $\nu = 3.3 \times 10^{-6}\,m^2/s$, and we simulated three cardiac cycles using the second-order finite element Navier–Stokes solver *Oasis* [30]. The waveform was taken from Hoi et al. [25], but scaled to match the average inlet flowrate, and set as Womersley flow with 20 modes. The time-step was set to 5×10^{-5} s, i.e., five times smaller than the time-step size at which we noticed effects of time resolution on the flow field, based on a spatio-temporal refinement study focused on turbulent-like flow [18]. The chosen time-step size matched the sampling frequency of the LDV in the experimental studies (20 kHz) [16].

Table 1 List of inflow and flow split set for each CFD simulation with several degrees of stenosis

Stenosis degree (%)	Q_{CCA} (ml/min)	(Q_{ICA}/Q_{CCA}) (%)	Category
None	**389**	**65.5**	Degree of stenosis
56	**337**	**58.8**	
66	**337**	**57.8**	
76	**337**	**45.0**	
86	**337**	**28.0**	
96	**152**	**11.9**	
76	**145**	45.0	Flow rate
76	**241**	45.0	
76	**433**	45.0	
76	**529**	45.0	
76	337	**18.0**	Flow split
76	337	**32.0**	
76	337	**58.0**	
76	337	**72.0**	
None	**315**	**54.5**	
None	**315**	**65.5**	Healthy flow split
56	**241**	**70.8**	combination
66	**337**	**44.4**	
76	**279**	**45.0**	
86	**337**	**28.8**	
86	**433**	**28.0**	

The text in bold is the parameters changed in each category. Note that the average flowrate and flow split changes with degree of stenosis, and is therefore not constant in the "degree of stenosis" category.

2.2 Postprocessing of Computational Data. The postprocessing workflow is depicted in Fig. 2 and can be described by the following steps:

(a) We extracted the pressure during the two last cardiac cycles at a point **P**, located on the centerline of the ICA, 8 mm downstream of the stenosis (see Fig. 1), as it was find to be the most relevant measuring location among the ones tested in vitro.
(b) The power of the pressure trace (P) was then computed in LabChart Pro v8. The fast Fourier transform was calculated from 1000 points with Hann windowing with 50% overlap.
(c) The integral of P was computed in Excel (Microsoft, 2016) using the trapezoidal rule within the frequency range of interest $[f_{min}, f_{max}]$. Unless otherwise reported in the contextual section, the default f_{min} value was set to 20 Hz to exclude the pulsatility of the inlet waveform only, and f_{max} was set to 10 kHz to encompass the entire available frequency range.
(d) Finally, we computed the logarithm of the integral, equivalent to a metric of the intensity of flow instabilities ($IFI_{[f_{min}, f_{max}]}$), that can be mathematically expressed as in the following equation:

$$IFI_{[f_{min}, f_{max}]} = Log_{10}\left(\int_{f_{min}}^{f_{max}} P\right) \tag{1}$$

Furthermore, for visualization purposes only, we performed a high-pass filter on the pressure trace with cut-off frequency at 20 Hz, in order to provide a qualitative representation of the pressure fluctuations. The method was previously explained in Ref. [18] and based on the study reported by Khan et al. [31].

For volumetric visualization, we also computed the Q-criterion, which identifies spatial regions in the velocity field where the Euclidean norm of the vorticity tensor (**Ω**) dominates the strain rate tensor (**S**) [32], as defined in the following equation:

$$Q = \frac{1}{2}\left[|\mathbf{\Omega}|^2 - |\mathbf{S}|^2\right] \tag{2}$$

2.3 Validation Against Experimental Data. A brief overview of the experimental methodology is reported to allow a better understanding of the validation strategy; details are found in Mancini et al. [16]. The in vitro setup consisted of a compliant

Table 2 List of inflow and flow split set during the in vitro experiments to allow validation of the CFD approach by comparing the simulations in the "flowrate" and the "degree of stenosis" categories, for the 76% stenosis only

Stenosis degree (%)	Q_{CCA} (ml/min)	$\frac{Q_{ICA}}{Q_{CCA}}$ (%)	Category
76	107	36.4	EXP
76	225	44.8	
76	334	47.1	
76	448	48.1	
76	601	48.7	

In the experiments, the ICA flow split was kept as close as possible to the mean physiological value, while the CCA flowrate was varied as within the physiological range by setting it at mean, ± 1 SD and ± 2 SD ml/min.

replica of a 76% stenosed patient-specific carotid bifurcation, the same geometry used in this study, embedded in a soft-tissue mimicking gel and a skin-mimicking polyurethane foil on top of it. LDV measurements were acquired at several locations upstream and downstream the stenosis. The displacement recorded using LDV in the in vitro experiments is, from now on, referred to as EXP. The LDV was found to be most sensitive to flowrate changes at a location corresponding to point **P**, which was therefore deemed the most relevant.

For comparison with the CFD data, we chose a subset of the in vitro experiments where the CCA flowrate was within mean±2 SD of clinically observed flow rates [23] and mean ICA flow split [24] (see Table 2) in order to compare them with the simulations in the "flowrate" category. Note that the CCA flowrate of the two datasets is in the same range, but not exactly matching because of the difficulty of controlling the flow rates during the in vitro experiments.

It is worth noticing that the two datasets are not directly comparable, as the experimental displacement was measured at the surface of a deformable and gel-surrounded model, while the intra-arterial pressure traces are obtained in a rigid model by a CFD solver. Therefore, a measure of the power of the two signals, i.e., $IFI_{[20\,Hz-10\,kHz]}$, was computed for the experimental data as well, with the same postprocessing process applied to the CFD data (summarized in Eq. (1)). We assessed the similarity of the skin-mimicking foil displacement and intra-arterial computational pressure by computing the correlation of $IFI_{[20\,Hz-10\,kHz]}$ at point **P** in the two datasets and, therefore, obtaining a concordance correlation coefficient.

2.4 Metrics Correlating With Flow Instabilities. To assess which metric best correlates with the level of flow instabilities, we performed six linear regression analyses between $IFI_{[20\,Hz-10\,kHz]}$ of the stenosed geometries ($IFI^{stenotic}_{[20\,Hz-10\,kHz]}$) and a total of six parameters, specifically the three imposed parameters (Q_{CCA}, Q_{ICA}/Q_{CCA}, and $Area_{stenosis}$, the area of the stenosis) and three derived quantities, i.e., Q_{ICA}, the velocity ,and Reynolds number at the throat of the stenosis ($Velocity_{stenosis}$ and $Re_{stenosis}$, respectively). The derived quantities were chosen based on their relevance in a fluid dynamical context. The quantity that was found to best correlate with the presence of flow instabilities is now referred to as *metric*. The regression analysis between the six quantities and $IFI^{healthy}_{[20\,Hz-10\,kHz]}$ was also computed for the healthy geometry, allowing us to identify the key indicators to distinguish a normal carotid from a stenotic.

2.5 Proof-of-Concept for Sensitivity, Specificity, and Accuracy of an Laser Doppler Vibrometer Device for Stenosis Detection. Sensitivity, specificity, and accuracy are commonly used to assess the predictive performance of a device or a method based on data of patients enrolled in a clinical trial. Clinical measurements, however, are subject to many disturbing cofounders, which is something that simulated data are immune to. Therefore, we took advantage of the computational data to provide a proof-of-concept on the feasibility of LDV to differentiate a stenosis from the normal setting in the tested geometry using power spectral features. Specifically, we used the IFI metrics within the frequency range identified by the in vitro experiments (0 − 200 Hz). Preliminary analysis of CFD results demonstrated that the IFI of a stenosis was low (absence of flow instabilities) either because of the geometry that was insufficiently stenosed, or because of how limiting severe stenosis act on the flowrate. We, therefore, choose to investigate two sets of frequency ranges, specifically the 0 – 40 Hz and the 80 – 200 Hz ranges, where the former would allow us to assess the flowrate level, and the latter the intensity of flow instabilities. The choice of the frequency ranges is properly addressed in the Results section under "Frequency-based stenosis indicators."

Furthermore, to enable a sensitivity and specificity analysis, additional data are required beyond the data obtained from the 21 CFD simulations. Therefore, we used the data from the 21 simulations to create a regression model that allowed us to create a fictitious population of 50,000 subjects, varying the parameters (CCA flowrate and ICA flow split) with five equally large subgroups for each degree of stenosis, and an additional 10,000 fictitious subjects without any ICA stenosis. For each fictitious subject, we drew a random point with coordinates (x, y) from a multivariate distribution, with covariate matrix equal to identity matrix and null mean, and assigned a CCA flowrate and an ICA flow split as $Q_{CCA} = (Q_{CCA})_{mean} + x \cdot (Q_{CCA})_{SD}$ and $Q_{ICA}/Q_{CCA} = (Q_{ICA}/Q_{CCA})_{mean} + y \cdot (Q_{ICA}/Q_{CCA})_{SD}$, respectively. The distribution coordinates x and y vary between −2 and +2 units in order to represent a population varying between ±2 SD. The mean and standard deviation values are dependent on the degree of stenosis, following [23–25], and reported in Table 1 category "degree of stenosis." Physiologically nonplausible conditions (i.e., $Q_{CCA} < 0$ and $Q_{ICA}/Q_{CCA} < 0$) were omitted, giving a final fictitious population of 45,756 patients and 9116 controls with $Q_{CCA} = 298 \pm 107$ ml/min and $Q_{ICA}/Q_{CCA} = 0.40 \pm 0.21$ across all degrees of stenosis, and $Q_{CCA} = 388 \pm 65$ ml/min and $Q_{ICA}/Q_{CCA} = 0.655 \pm 0.1$ for the healthy model.

Based on the geometrical and flowrate information of each fictitious subject, we could compute all the potential metrics for the entire fictitious population. We then correlated the metric with $IFI_{[f_{min}, f_{max}]}$ to obtain the regression coefficients for each frequency range, and therefore computed an approximation of $IFI_{[f_{min}, f_{max}]}$ ($\tilde{IFI}_{[f_{min}, f_{max}]}$) for each fictitious subject without running a full CFD simulation. Of note is that the regression coefficients were computed separately for the 18 stenotic models and for the three healthy ones, for each relevant frequency range.

Finally, we performed a receiver operator characteristic (ROC) analysis [33] to evaluate the ability of $\tilde{IFI}_{[f_{min}, f_{max}]}$, evaluated at both frequency ranges, to infer the presence of a carotid artery stenosis. We varied the cut-off value from min to max of each $\tilde{IFI}_{[f_{min}, f_{max}]}$ and computed the rate of true positives (TP_{rate}), and the rate of false positives (FP_{rate}), equivalent to sensitivity (Sn) and 1–specificity (Sp), respectively. The accuracy of the test was calculated as the area under the curve (AUC) of the ROC curve by means of the trapezoidal rule. We chose the optimal cut-off value based on the Youden Index [34], defined as $J = \max_c (Sn(c) + Sp(c) - 1)$.

3 Results

3.1 Computational Findings. An overview of the velocity field of the "flowrate" category is shown in Fig. 3 to allow for a qualitative analysis of the well-resolved physics of our computational methodology.

The velocity traces in point **P** (Fig. 3(*a*)) and the volumetric rendering of the instantaneous velocity magnitude field at $t = T/4$ (Fig. 3(*b*)) are reported for increasing Q_{CCA} (Fig. 3(*c*)). The pressure fluctuations in the ICA increase proportionally to the CCA flowrate, as highlighted by the high velocity jet emerging from the throat of the stenosis. The increased velocity leads to the

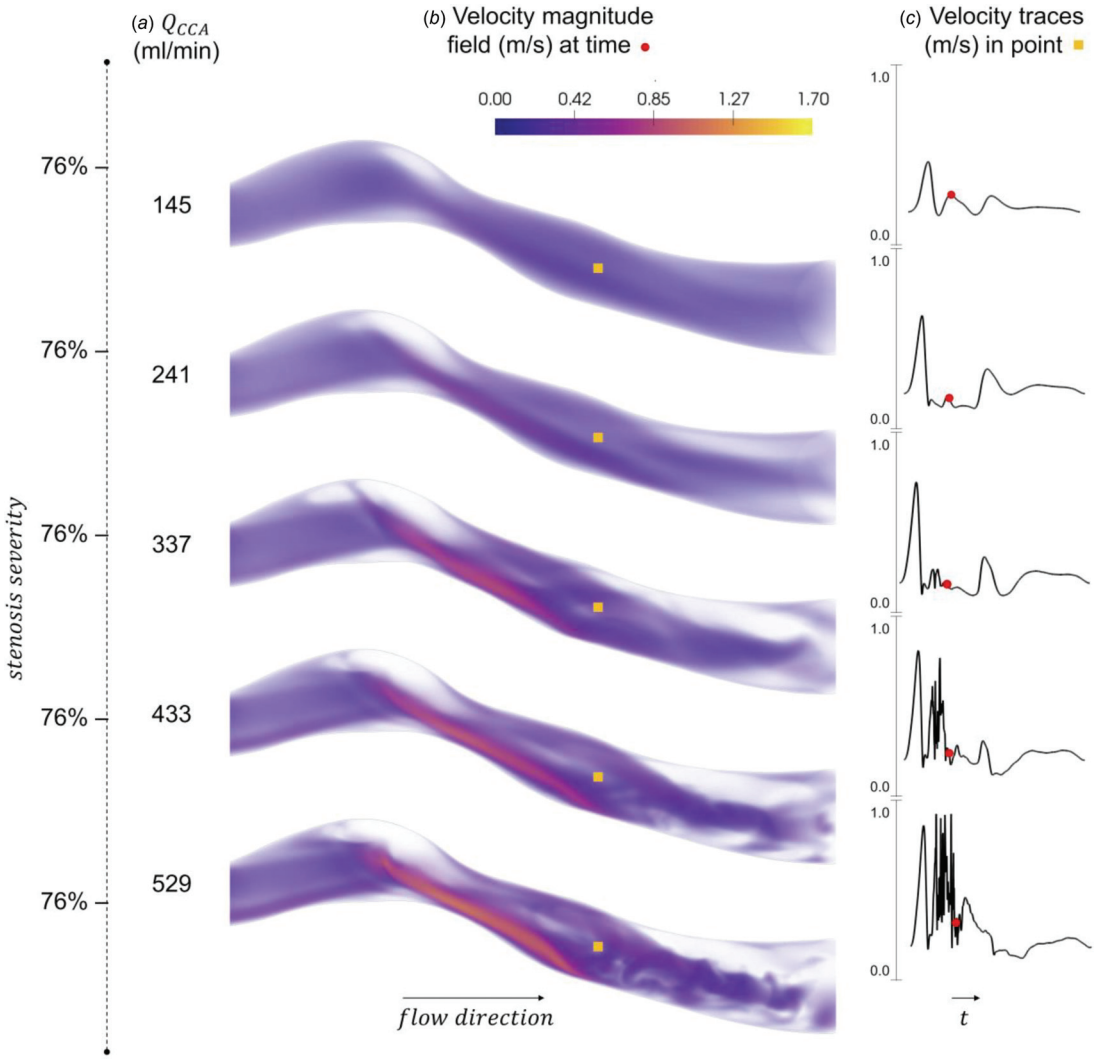

Fig. 3 An increase in Q_{CCA} (*a*) leads to noticeable increase of velocity magnitude (*b*) and of flow instabilities (*c*) for the 76% stenosis. The velocity traces in (*c*) were sampled in point *P* (yellow square), and the volumetric velocity magnitude in (*b*) was sampled at a fourth of the cardiac cycle (red dot). Higher Q_{CCA} implies higher velocity values at the stenosis throat, which trigger vortexes in the downstream region.

formation of flow instabilities in the more distal ICA. The combined effect of increased velocity magnitude and its subsequent effect on the intensity of flow instabilities are clearly noticeable in the velocity traces of Fig. 3(*a*).

3.2 Validation Against In Vitro Experiments. The traces of normalized computational pressure data and normalized experimental displacement obtained using LDV recordings are compared in Fig. 4(*a*) where we can observe an increase in pressure drop and displacement magnitude with increasing flow rates. As expected, the raw data of the two datasets are not directly comparable one to the other.

The instabilities in the LDV signal are masked by its high amplitude. We, therefore, report the high-pass filtered signals in Fig. 4(*b*) for a visual proof of the presence of flow instabilities. From the high-pass filtered pressure signals, we observe that for the two lowest flow rates there are little to no high-frequency instabilities. In contrast, the high-pass filtered displacement traces for the three higher flow rates contain an increasing level of fluctuations. However, for both datasets, the fluctuations are present and increase with the flowrate, and the same applies to their power, shown in Fig. 4(*c*). Furthermore, the logarithm of their integral in the 20 Hz–10 kHz range, shown in Fig. 4(*d*), displays a similar linear trend, increasing with Q_{ICA}, suggesting that the intensity of the pressure fluctuations, as obtained from the CFD simulations, can be used as a proxy for the intensity of wall vibrations as measured with LDV. It is worth noticing that the data points in Fig. 4(*d*) are plotted on separate *y*-axes, since we are comparing two different physical quantities. The two datasets were found to be in good agreement, with a concordance correlation coefficient of 0.9819. We can, therefore, conclude that our computational methodology provides plausible results for the patient-specific 76% stenotic model. We could hence use CFD simulations to investigate a larger set of parameters.

3.3 Metrics Correlating With Flow Instabilities in Stenosed and Healthy Models. In this section, we report the results of the correlation between the $IFI_{[20\,Hz-10\,kHz]}$ and six parameters describing the flow and stenosis geometry. Specifically, Figs. 5(*a*)–5(*c*) show the correlation of the three imposed parameters (Q_{CCA}, Q_{ICA}/Q_{CCA} and $Area_{stenosis}$) with $IFI_{[20\,Hz-10\,kHz]}$. Figures 5(*d*)–5(*f*) show the correlation of $IFI_{[20\,Hz-10\,kHz]}$ with the three obtained parameters (Q_{ICA}, $Velocity_{stenosis,}$ and $Re_{stenosis}$). The stenotic and the healthy models are analyzed separately to ease comparison between them. An increase in any of these parameters generally leads to an increase of the intensity of flow instabilities. Focusing first on the stenotic models, the stenosis area was the only factor where the slope of

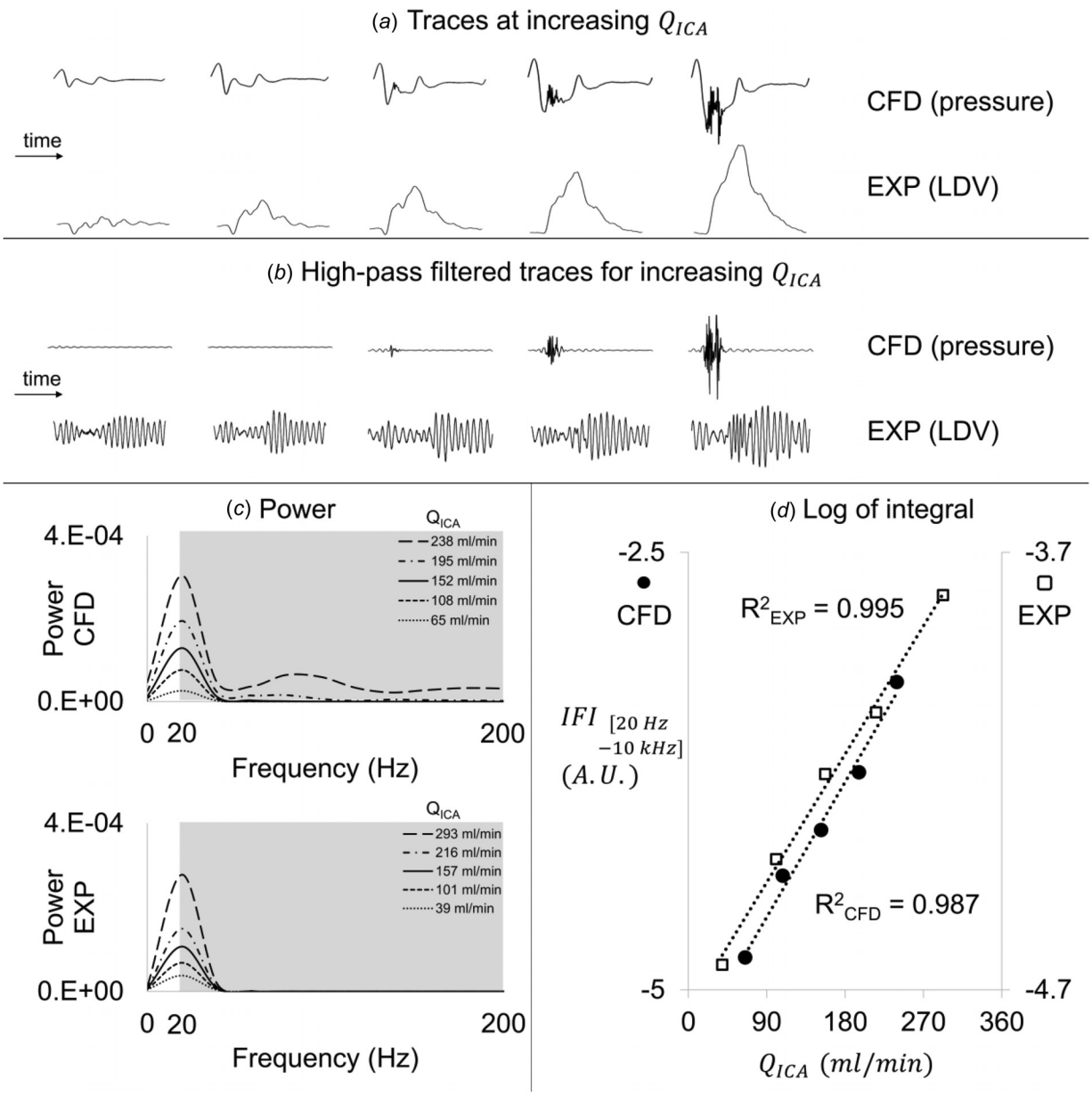

Fig. 4 (*a*) The pressure obtained from the computational simulations is compared to the LDV displacement obtained from experimental tests at increasing Q_{ICA} (whose values are reported in the legends of panel c). The displacement increased in amplitude as the flowrate in the stenosed vessel increased, which lead as well to an increase of instabilities in the pressure field. The increase of instabilities with ICA flowrate is highlighted by the high-pass filtered time traces (*b*) and their power (*c*) of both the CFD and EXP data. Similarly, the scatter plot (*d*) shows that $IFI_{[20\,Hz-10\,kHz]}$ from both CFD and EXP data tend to increase together with Q_{ICA}. The gray box in (*c*) highlights the frequency range (20 Hz to 10 kHz) in which the IFI shown in (*d*) is calculated.

the regression line was not significantly different from zero with $p-$value > 0.05 and was a poor metric for IFI, accounting for only 15% of the variation in the data. The correlation improved for Q_{CCA}, $\text{Velocity}_{\text{stenosis,}}$ and Q_{ICA}/Q_{CCA}, with $R^2 = 0.39$, 0.56, and 0.54, respectively; but only Q_{ICA} and $\text{Re}_{\text{stenosis}}$ have an R^2 value of 0.90. For the sake of conciseness, we here report the results of the following analysis performed only for Q_{ICA} as metric, as Q_{ICA} is more relatable to measurements in the existing literature and clinical practice. The Q_{ICA} was also found to be the best metric for the increase of IFI for the healthy models as well, comparable to $\text{Velocity}_{\text{stenosis}}$ and $\text{Re}_{\text{stenosis}}$.

It is worth noticing that the linear correlation between most of the considered flow metrics and the IFI, computed as the logarithm of the energy integral, suggests that the parameters actually correlate exponentially with the intensity of flow instabilities.

A qualitative evaluation of the intensity of flow instabilities is provided using the high-pass filtered pressure signals, shown with the corresponding Q_{ICA} value in Fig. 6. The simulations are depicted for increasing Q_{ICA} values. Of note is that the 96% stenosis does not harbor flow instabilities, because of our physiology-based boundary conditions. The 86% stenosis harbors weak instabilities only if the flowrate is above average, while the fluctuations harbored with average Q_{CCA} are negligible. The 76% stenosis simulations exhibit a phenotypically different behavior depending on the flow split and inlet flowrate. More specifically, a high flow split or inlet flowrate (average + 2 SDs) produced the most unstable flows, while the simulations with a reduction below the average of these parameters did not harbor high-frequency pressure fluctuations. The 66% and 56% are slightly unstable through the entire range of physiological CCA flowrate or flow split used in this study. The high-pass filtered pressure traces of

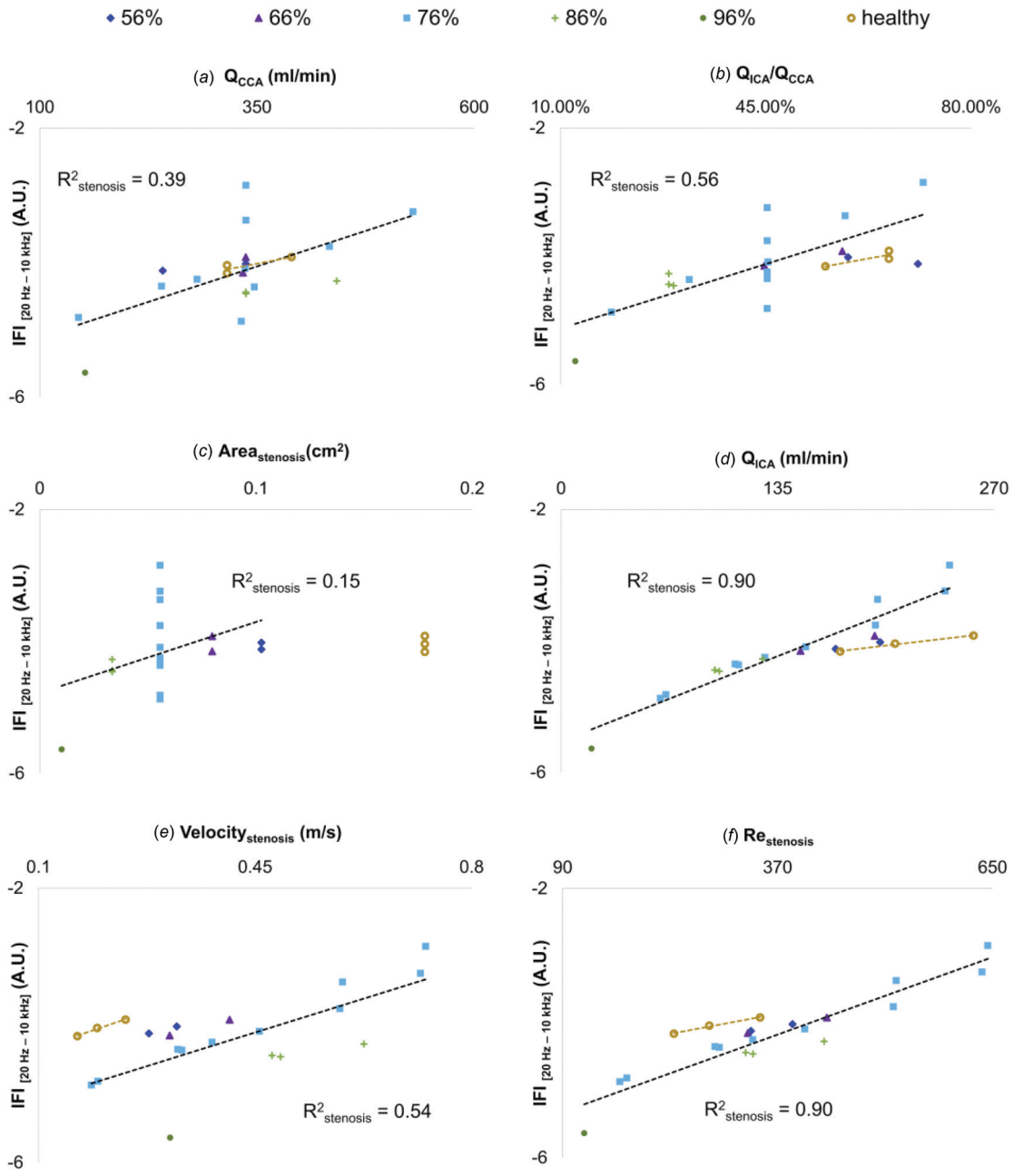

Fig. 5 The impact of the physiologically relevant factors (Q_{CCA}, Q_{ICA}/Q_{CCA}, $Area_{stenosis}$, Q_{ICA}, $Velocity_{stenosis}$, and $Re_{stenosis}$) on the intensity of flow instabilities is depicted in separated plots. The regression analysis was performed for the stenotic and the healthy models separately. All factors are positively related with $IFI_{[20\,Hz-10\,kHz]}$ but their correlation varies between a minimum of 0.15 for $Area_{stenosis}$ and a maximum of 0.90 for Q_{ICA} and $Re_{stenosis}$.

the healthy model simulations are highlighted with a gray box. The healthy model does not show any flow instabilities, even though the Q_{ICA} would have been high enough to trigger flow instabilities in any of the stenotic models ($Q_{ICA} = 257\,ml/min$). Similar considerations can be drawn when evaluating the high-pass filtered pressure traces (a) and the Q-criterion (b) in the healthy model simulation, together with Q_{ICA} (c) for each stenosis degree in Fig. 7. Shifting our attention to the 56–76% stenosis models, it is possible to see flow vortexes both upstream, at, and downstream of the stenosis throat. The differences with the healthy model in both high-frequency pressure traces and vortexes are clearly noticeable. We find the lowest Q_{ICA} in the most severe stenoses (86% and 96%), where weak or no instabilities are present. The Q_{ICA} is hence a good metric for the presence of flow instabilities if a stenosis is present; otherwise, the geometrical factors have a predominant impact.

3.4 Frequency-Based Stenosis Indicators. Figures 6 and 7 suggest that the high-frequent flow instabilities can be used as indicator for the presence of the moderate stenoses (56–76%), but not for severe stenosis as a result of the reduced flow, which was too low to induce instabilities. Analysis of the high-frequency contents of the signal in itself, therefore, would be insufficient to infer the presence of stenosis. Additional information may be found in a metric that would indicate the flow level in itself, which will be markedly lower in case of severe stenosis (86% and 96%). Therefore, the power spectrum in the lower frequency range may

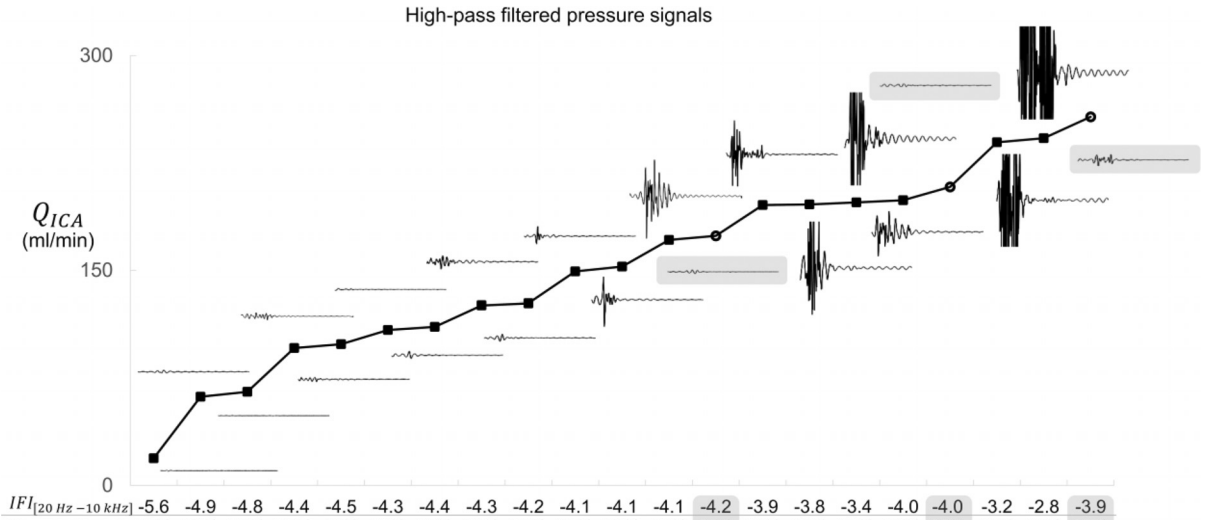

$IFI_{[20\,Hz-10\,kHz]}$	-5.6	-4.9	-4.8	-4.4	-4.5	-4.3	-4.4	-4.3	-4.2	-4.1	-4.1	-4.1	-4.2	-3.9	-3.8	-3.4	-4.0	-4.0	-3.2	-2.8	-3.9
Degree stenosis	96%	76%	76%	86%	86%	76%	76%	86%	76%	66%	76%	56%	00%	66%	76%	76%	56%	00%	76%	76%	00%
Q_{CCA} (ml/min)	152	337	145	337	337	241	337	433	280	337	337	241	316	337	433	337	337	316	529	337	390
Q_{ICA}/Q_{CCA}	0.12	0.18	0.45	0.28	0.29	0.45	0.32	0.28	0.45	0.45	0.45	0.71	0.6	0.58	0.58	0.58	0.59	0.7	0.45	0.72	0.7

Fig. 6 The incremental plot of Q_{ICA} highlights the positive relationship between the Q_{ICA} and the high-pass filtered pressure signals which, on the other hand, are largely insensitive to other expectedly relevant parameters such as stenosis severity, inlet flowrate and flow split. The $IFI_{[20\,Hz-10\,kHz]}$ is reported to show the difference between stenotic and healthy models' values. The high-pass filtered pressure signals obtained using the healthy model are highlighted with a gray box, showing that no flow instabilities arise even if their Q_{ICA} is in the range in which the stenotic models harbor intense instabilities.

provide this information. The left side of Fig. 8(*a*) illustrates that the majority of the energy related to the bulk flow is mostly present in the 0–40 Hz range, which was therefore chosen as the relevant frequency range for discerning severe stenoses from healthy carotid arteries. Furthermore, we observe that the power of the healthy and the severe stenoses reaches approximately 0 at 80 Hz, while the energy content of the moderate stenoses is non-negligible until 200 Hz. Therefore, the $IFI_{[80-200\,Hz]}$ could be used as indicator for the presence of moderate stenoses. The sensitivity and specificity of $IFI_{[0-40\,Hz]}$ and $IFI_{[80-200\,Hz]}$ for the detection of severe and moderate stenoses, respectively, were investigated in the following chapters.

3.5 Laser Doppler Vibrometer for Stenosis Detection: Proof-of-Concept. Based on these preliminary findings, we performed a total of four linear regression analyses between Q_{ICA} and the CFD-based IFIs, for stenotic and healthy models separately, with IFIs evaluated at both frequency ranges. The correlation was found to be high for all cases, with $R^2 > 0.89$, as reported in Table 3. The regression coefficients (Table 3) were used to obtain $\tilde{IFI}_{[0-40\,Hz]}$ and $\tilde{IFI}_{[80-200\,Hz]}$ from Q_{ICA} of the fictitious population.

The probability density functions of the fictitious population were evaluated for both frequency ranges and reported in Fig. 8(*b*). The probability density functions represent the distribution of the diseased and healthy groups, therefore, providing insights on the forecast probability of each classifier, i.e., $\tilde{IFI}_{[0-40\,Hz]}$ and $\tilde{IFI}_{[80-200\,Hz]}$. On the left side, the distribution of the healthy fictitious population overlaps only partially on the 86% stenosis, and not at all on the 96%, showing promising possibilities for the $\tilde{IFI}_{[0-40\,Hz]}$ as indicator for severe stenoses, but less so for moderate stenoses. On the other hand, the distribution of the healthy population obtained for $\tilde{IFI}_{[80-200\,Hz]}$ (Fig. 8(*b*), right side) overlaps only marginally with the moderate stenoses but almost completely the severe stenoses, showing that $\tilde{IFI}_{[80-200\,Hz]}$ could be used to identify moderate stenoses but not severe ones. Therefore, the probability density functions suggest that it could be possible to infer the presence of moderate and severe stenoses by using the $\tilde{IFI}$s evaluated at high and low frequency ranges, respectively, as classifiers. We, therefore, based our ROC analysis by evaluating $\tilde{IFI}$ in the 80 – 200 Hz and 0 – 40 Hz range, see Fig. 8(*c*), left and right panel, respectively. The reference probability line is added to both plots, showing that the accuracy of the $\tilde{IFI}$ s is higher than a predictor which makes random guesses (AUC = 0.50). As expected from the probability density functions plots, the ROC analysis shows that $\tilde{IFI}_{[0-40\,Hz]}$ infers the presence of severe stenoses with AUC = 0.97, while $\tilde{IFI}_{[80-200\,Hz]}$ infers the presence of moderate stenosis with AUC = 0.84. The AUC of each curve is reported in Table 4. From Youden index, we have that the optimal cut-off value is $\tilde{IFI}_{[0-40\,Hz]} = -3.96$ with Sp = 92% and Sn = 99%, and $\tilde{IFI}_{[80-200\,Hz]} = -6.91$ with Sp = 73% and Sn = 96%.

4 Discussion

Combining an experimental and a computational approach, we theoretically assessed the feasibility of stenosis detection with a device capable of measuring signals induced by flow instabilities, such as LDV, by evaluating their intensity in healthy and stenosed models. Starting from 21 high-resolution CFD simulations in models spanning a pathophysiological parameter range, we obtained a fictitious population. The intensity of flow instabilities was most strongly correlated with Q_{ICA}, the flowrate in the stenosed vessel ($R^2 = 0.90$). A ROC analysis suggests that vibrations measured with an LDV device may reveal severe and moderate stenoses with sensitivity and specificity > 73%, by evaluating the IFI at two frequency ranges, i.e., 0 – 40 Hz and 80 – 200 Hz, respectively. The use of two frequency bands is needed because the flow-limiting character of severely stenosed models leads to negligible flow instabilities and the low-frequency range power amplitude would allow us to distinguish them from the healthy models. Overall, this study supports the development of diagnostic techniques relying on detecting and processing of signals arising from flow instabilities for the detection of moderate and severe stenoses.

4.1 Validation Strategy. The results in this paper were based on using the computed pressure traces as proxy for wall

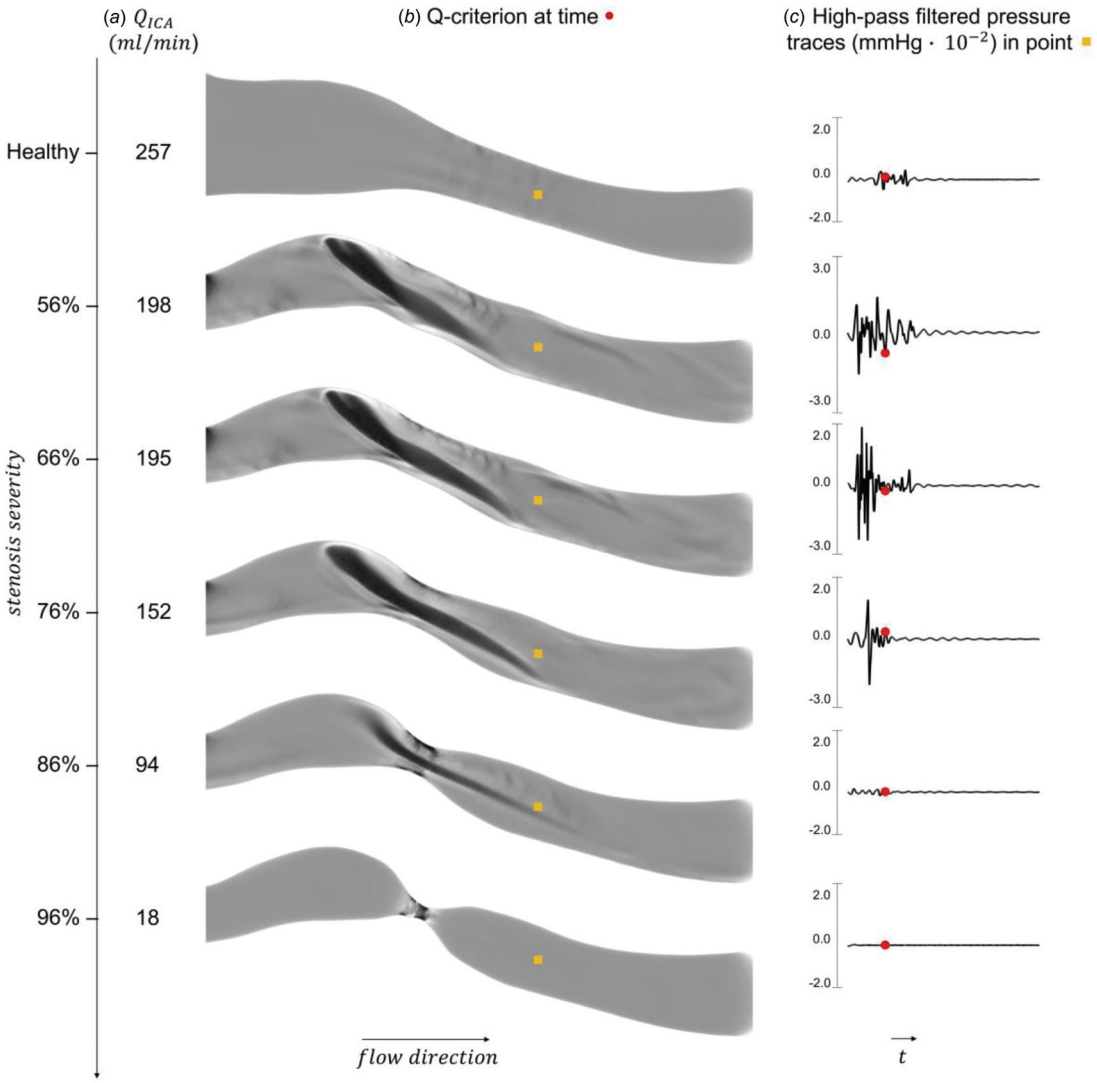

Fig. 7 The used Q_{ICA} is reported (*a*) in correspondence of the vortexes in the ICA region, identified using the *Q*-criterion (*b*), of each model (category "degree of stenosis"). The volumetric rendering of the *Q*-criterion was obtained at a fourth of the simulated cycle, highlighted by the red dot on the high-pass pressure traces displaced in panel (*c*), which were obtained at point *P* (yellow square). As expected, the jet of the flow does not break down when entering the stenosis in the healthy geometry, while numerous vortexes arise in the 56%, 66%, and 76% stenoses. The flow in the 86% stenosis is also unstable but less than the 56−76% stenoses. In the 96% geometry, on the other hand, the weak instabilities dissipate closely downstream of the narrowing.

vibrations, which we validated against in vitro data. The correlation between the two datasets is 98.19%.

Interestingly, the IFI was found to be unaffected by which physical quantity it was calculated from. The experimental data referred to displacement recorded using LDV on the surface of a soft-tissue-mimicking gel, which embedded a compliant replica of the carotid arteries. The computational data, on the other hand, consisted of pressure fluctuations. During the experiments, in vitro intra-arterial pressure was also measured. However, the presence of pressure catheters significantly affected the flow field and thereby made any comparison with the simulated flow field not relevant.

Our findings also suggest that the material properties of the compliant experimental model and the rigid-walls computational model did not affect the turbulent flow field, as similar flow fields were obtained from the two datasets. Note also that, despite the mentioned differences, the characteristic frequencies for the turbulent-like flow are in the <200 Hz region for both the numerical and experimental data [16].

4.2 Computational Model. Using our computational resources, we were able to evaluate the flow field of several stenosis severities throughout 21 CFD simulations, specifically 18 for the stenosed models and 3 for the healthy one.

There have been multiple CFD studies performed on a cohort of patients affected by carotid stenosis [35,36]. However, they mainly focused on wall shear stress and disease progression. To the best of our knowledge, this is the first study focusing on how the intensity of turbulent-like poststenotic flow varies with flowrate, flow split, and degree of stenosis. This study was limited to a Newtonian formulation of the blood, but the effect of using a non-Newtonian fluid on the flow field of the carotid bifurcation was found to be negligible, due to the high shear rates that force the models to work in a quasi-constant viscosity regime [37]. Furthermore, Khan et al. [28,29] observed that assuming viscosity as a constant value has a negligible practical impact on the turbulent flow field.

4.3 Healthy Control. Another important aspect of this paper was the comparison between the healthy and diseased models.

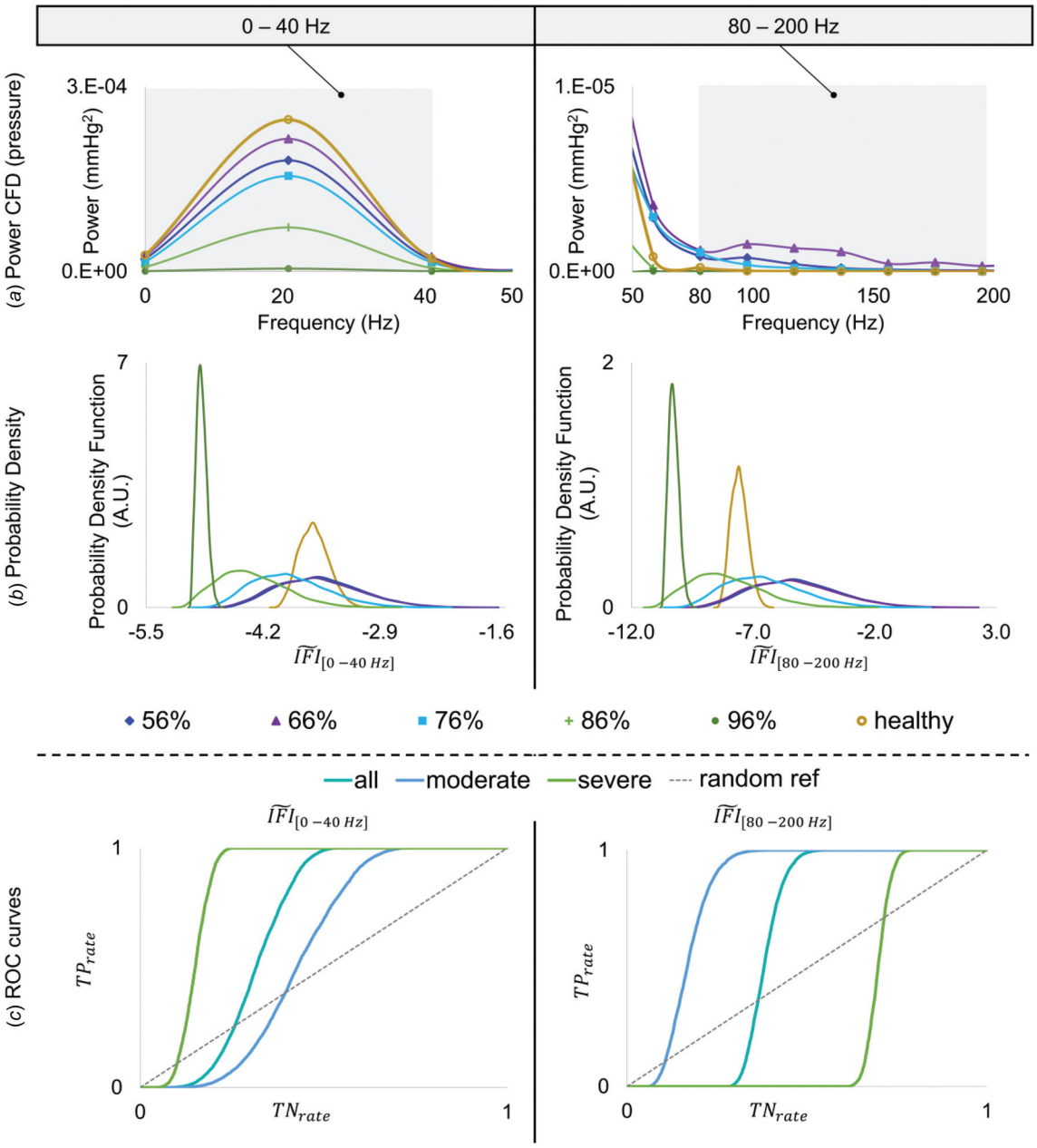

Fig. 8 The CFD data evaluated in the 040 Hz and in the 80200 Hz ranges are reported on the left and right side, respectively. (*a*) The power of the pressure fluctuations obtained from the six CFD simulations in category "degree of stenosis" (mean Q_{CCA} and Q_{ICA}/Q_{CCA}) is plotted in two frequency ranges (identified by the gray boxes), highlighting a difference in the energy content of the moderate (56%, 66%, and 76%) and severe (86% and 96%) stenoses. (*b*) The probability density distributions, obtained from the extended population by means of regression analyses in each range, show that by evaluating IFI in two separate frequency ranges, it is possible to distinguish the moderate and severe stenoses from the healthy model. (*c*) The ROC curves show that the accuracy of severe and moderate stenosis prediction using $\widetilde{IFI}_{[0-40\,Hz]}$ and $\widetilde{IFI}_{[80-200\,Hz]}$, respectively, is higher than the one of a random predictor with 50% chance of detection.

The healthy model did not harbor flow instabilities despite the relatively high Q_{ICA}, showing how strongly the presence of a stenosis affects the flow field. Of note is that the flow field in the healthy model was different already upstream of the area where the stenosis would occur, as due to the growth of the atherosclerotic plaques. The computer tomography angiography images [19] showed the presence of hypo-cellular and calcified plaques spread along the ICA since its attachment to the carotid bifurcation, highlighting that what we consider a stenosis is actually the location with the most extreme narrowing. It is well known that the arteries of patients affected by atherosclerosis are overall narrower than the same artery prior to the growth of the plaque. Consequently, the differences in fluid dynamics among a healthy and a stenotic patient are even more marked, explaining the absolute absence of vortexes in the healthy model despite the comparable Q_{ICA}.

4.4 Reynolds Number. As expected, the linear regression analysis between Q_{ICA} and $IFI_{[f_{min}, f_{max}]}$ in the 20 Hz − 10 kHz range showed that the Reynolds number is an equally good correlation metric for the presence of flow instabilities as Q_{ICA}. Despite its limited use in the clinical practice, the $Re_{stenosis}$ is still relevant

Table 3 The correlation between Q_{ICA} and $IFI_{[f_{min}, f_{max}]}$ evaluated at the two frequency ranges was found to be extremely high ($R^2 \geq 0.89$)

Frequency range	Model	R^2	a	B
$f_{min} = 0$ Hz	Stenotic	0.89	0.007386632	−5.016398344
$f_{max} = 40$ Hz	Healthy	0.99	0.002858473	−4.360716439
$f_{min} = 80$ Hz	Stenotic	0.89	0.028025848	−10.7696061
$f_{max} = 200$ Hz	Healthy	0.96	0.006015117	−9.095393066

The regression coefficients (a, b) were used to obtain the $\widetilde{IFI}$ values in both frequency ranges and for each subject of the fictitious population using the expression $\widetilde{IFI}_{[f_{min}f_{max}]} = a \cdot Q_{ICA} + b$.

Table 4 The accuracy of the IFI in the 0−40 Hz range shows that it is a good predictor for severe stenoses, while it is poorly accurate for moderate stenoses detection

Stenosis degree	AUC based on $IFI_{[0-40\,Hz]}$	AUC based on $IFI_{[80-200\,Hz]}$
Moderate (56 %, 66 %, 76 %)	0.559	**0.843**
Severe (86 %, 96 %)	**0.972**	0.162
All (56 − 96 %)	0.726	0.569

In the 80−200 kHz range, on the other hand, the IFI can infer the presence of moderate stenoses and, with lower accuracy, of the severe stenoses too.

from an engineering point of view. We therefore performed the ROC analysis using $Re_{stenosis}$ as metric for IFI evaluated at same frequency ranges as Q_{ICA}. We found that there was little to no impact on sensitivity and specificity, as the results were in agreement with those obtained with Q_{ICA}, with AUC = 0.82 and 0.85 for moderate and severe stenoses, respectively. Thus, as expected, confirming the strong correlation between $Re_{stenosis}$ and the intensity of flow instabilities at any stenosis degree.

4.5 Fictitious Population. Using the linear regressions, we could create a fictitious population and perform ROC analyses. We did this considering two frequency bands: $\widetilde{IFI}_{[0-40\,Hz]}$ and $\widetilde{IFI}_{[80-200\,Hz]}$. Of note is that nine additional frequency bands were considered, ranging within the entire simulated frequency domain (0 – 10 kHz), but our data indicates that the 0 − 40 Hz range best reveals information on the flowrate, while the higher 80 − 200 Hz frequency band finely reveals the presence of flow instabilities. In our analysis, both were needed to discriminate a stenosed from a nonstenosed vessel because of the flow limiting character of severe stenosis. Indeed, when using $\widetilde{IFI}_{[80-200\,Hz]}$, the curve for severe stenoses is consistently below the 50% probability reference line.

We found low sensitivity when detecting extremely severe stenoses using flow instabilities, which agrees with several clinical studies. For instance, the sensitivity for auscultation of asymptomatic carotid stenosis was found to be 29% by Johannson and Wester [38]. McColgan et al. also noticed that the likelihood of carotid bruit does not increase with stenosis degree [9]. These findings suggest that evaluations based on carotid bruits, i.e., flow instabilities, and are not sufficient to exclude the presence of extremely severe carotid stenosis.

However, it is worth noticing that by combining the $\widetilde{IFI}_{[80-200\,Hz]}$ and $\widetilde{IFI}_{[0-40\,Hz]}$ data, and using a simple linear classifier, we were able to achieve a perfect classification of our fictitious population, i.e., AUC = 1.0 and a specificity and sensitivity of 100%.

4.6 Future Work. Verification and validation of computer models have been a subject of struggle for the modeling and simulations community since the 1960s [39]. If applicable, comparisons should be made using well-known benchmarks or well-understood techniques in order to accurately quantify the uncertainties [40]. The U.S. Food and Drug Administration (FDA) designed a nozzle benchmark for the validation of CFD models applied to generic medical devices [41], and asked the CFD community to perform validation simulations in 2008–2009. However, a large interlaboratory disagreement was found in the predicted breakdown location of turbulent jet for transitional flow regimes. Several studies argued that the discrepancy was due to the lack of measured boundary conditions, which prevented numerical reproducibility [42], as the experimental noise could have triggered the onset of turbulence whereas the idealized boundary conditions would not [43]. It is indeed well established that the environment in which validation experiments are conducted, as being the quantification of the ability of a computer model to replicate the physics of the investigated problem their primary purpose, should be carefully controlled and measured in order to guarantee interlaboratory repeatability [40]. In this context, our validation strategy lacked on the numerical reproducibility as much as the FDA benchmark did, as the computational boundary conditions set in our models are based on idealized values as well. Our primary purpose, however, was restricted to the validation of a single computer model whose specific purpose was to obtain a set of intensity of flow instabilities large enough to allow a statistically significant analysis of the ability of an LDV device to detect stenosis. As such, we were not interested in the absolute value of IFI, but rather in the correlation to geometric and flowrate parameters, i.e., Q_{ICA} or $Re_{stenosis}$. In order to encourage further discussion on the subject and promote openness in science, we point out the availability of the experimental dataset in an online repository [44].

The pressure traces show that flow instabilities are particularly intense after the systolic peak, and almost never present in the diastolic phase of the cardiac cycle. Future work may also consider performing a temporal analysis of the traces, focusing on specific moments during the cardiac cycle, to look for frequency-dependent features.

We obtained the fictitious population on which the ROC analysis was performed by using the correlation coefficients of the Q_{ICA} of 21 CFD simulations (18 stenotic, three healthy) and the IFI. Obviously, the number of CFD simulations included in this study had an immediate impact on the accuracy of the correlation. The number of simulations was kept as small as possible due to the surge of CPU hours demanded by each additional one. It is practically unfeasible to run enough simulations to cover all combinations of CCA flowrate, ICA flow split, and stenosis degree. A larger set of simulations run on a broader population could allow for a more accurate estimate of the correlation coefficients. We made sure to run at least two simulations per stenosis degree, in order to improve the reliability of our regression model as predictor for the presence of carotid stenosis. Exceptionally, we included only one simulation run on the 96% stenosis model because no difference in IFI was noticeable when increasing the Q_{CCA} to 2 SD (i.e., $Q_{ICA} = 27$ ml/min), suggesting that the extremely severe stenosis could not harbor flow instabilities in physiologically varying ICA flow rates. Furthermore, we run only three simulations with the healthy model as a consequence of the choice to investigate only the flowrate levels appropriate for stenotic models. It is worth noticing, however, that small flow instabilities were found in the healthy model for ICA flow rates on the high side of its physiological range $Q_{ICA} = 351.8$, corresponding to + 2 SD.

The sensitivity and specificity measured in our fictitious feasibility studies outperform clinical studies using auscultation. The association between carotid bruit, related to the presence of flow instabilities, and carotid stenosis was found to have an average Sn = 53% and Sp = 83% over 26 clinical studies [9]. Although our results are more encouraging than previous in vivo studies, we have to point out that our study excludes all the variation from patient-specific geometry and neck skin properties. The findings

in this study are based on only one set of patient-specific clinical images, with its unique tortuosity and plaque morphology. Patient-specific anatomical aspects such as curvature, nonplanarity and tortuosity of carotid arteries, and the distance of the ICA stenosis from the carotid bifurcation, might have an impact on the onset of flow instabilities, and on the identified frequency bands and metrics. Caution is therefore warranted in interpreting the findings and a further extension of the study with additional patient-specific data would strengthen the theoretical basis. At the same time, the proof-of-concept character of the work should be kept in mind, where we wanted to explore the discriminative power of a frequency-domain analysis of features induced by poststenosis flow instabilities in an experimental and CFD model. The effective sensitivity and specificity of the technique will always have to be based on an in vivo study, irrespective of any computational study.

In this study, we assess the interpatient variability of IFI values. However, when performing in vivo measurements, it might be more relevant to quantity the intrapatient variability of IFI values by comparing the measurement obtained from both carotid arteries. From a mathematical point of view, this would be a "patient-specific" normalization of the data, which hopefully would reduce the impact of geometry and neck skin properties.

Finally, caution is warranted when interpreting our results from the collection of fictitious subjects. Our approach is only intended as a rough estimate of the sensitivity and specificity for each degree of stenosis. One cannot draw any direct clinical conclusions from these results, but could help guiding future exploratory clinical trials. Furthermore, given the intrinsic limitations of in silico and in vitro studies, the effective potential of this theoretically validated technique should be followed up and validated by clinical studies. If our feasibility results would be found to be applicable in vivo, the use of such device in the clinical practice could improve early carotid stenosis detection.

5 Conclusions

We have performed CFD simulations in a patient-specific carotid bifurcation geometry in order to evaluate the feasibility of LDV to infer carotid stenosis. Specifically, we evaluated the flow field obtained by different degrees of stenosis in the internal carotid artery, subjected to boundary conditions spanning the physiological range. We introduced the IFI as a measure to quantify the intensity of downstream fluctuations. We have demonstrated that the flowrate in the stenosed artery is a major determinant of downstream flow instabilities, which arise quite intensely in moderate stenoses (56–76%). Interestingly, bulk flow could also be used to identify the most stenotic carotid arteries. The accuracy of moderate and severe stenoses detection by means of an LDV device was found to be encouraging. Noticeably, the pressure-based CFD analysis parallels the analysis of experimental data in the same geometrical model embedded in a gel, where the relation between trans-stenotic flow and intensity of vibrations at the gel surface was studied. These results support the feasibility of the use of LDV to infer asymptomatic carotid stenosis, pending validation via clinical trials.

Acknowledgment

The study was done within the context of the H2020 European funded 644798 CARDIS project. We greatly acknowledge the contribution of the entire consortium and the teams behind the development and construction of the multi-array prototype.

This work was also carried out as a part of the Centre for Cardiological Innovation, and SIMMIS, project number 262827, funded by the Research Council of Norway. Computations were performed on the Abel Cluster, owned by the University of Oslo and the Norwegian metacenter for High Performance Computing (NOTUR), and operated by the Department for Research Computing at USIT, the University of Oslo IT-department, Grant No. nn9316k.

We also acknowledge the important contribution from the late professor Jan Vierendeels.

References

[1] GBD 2017 Causes of Death Collaborators, 2018, "Global, Regional, and National Age-Sex-Specific Mortality for 282 Causes of Death in 195 Countries and Territories, 1980–2017: A Systematic Analysis for the Global Burden of Disease Study 2017," Lancet, **392**(10159), pp. 1736–1788.

[2] Moomaw, C. J., Woo, D., Khatri, P., and Ferioli, S., 2013, "Carotid Artery Stenosis as a Cause of a Stroke," Neuroepidemiology, **40**(1), pp. 36–41.

[3] Naghavi, M., 2010, *Asymptomatic Atherosclerosis: Pathophysiology, Detection and Treatment*, Humana Press, Totowa, NJ.

[4] Hobson, R. W., Mackey, W. C., Ascher, E., Murad, M. H., Calligaro, K. D., Comerota, A. J., Montori, V. M., Eskandari, M. K., Massop, D. W., Bush, R. L., Lal, B. K., and Perler, B. A., 2008, "Management of Atherosclerotic Carotid Artery Disease: Clinical Practice Guidelines of the Society for Vascular Surgery," J. Vasc. Surg., **48**(2), pp. 480–486.

[5] Lanzino, G., Rabinstein, A. A., and Brown, R. D., Jr, 2009, "Treatment of Carotid Artery Stenosis: Medical Therapy, Surgery, or Stenting?," Mayo Clin Proc, **84**(4), pp. 362–368.

[6] Ahmed, S. A., and Giddens, D. P., 1983, "Velocity Measurements in Steady Flow Through Axisymmetric Stenoses at Moderate Reynolds Number," J. Biomech., **16**(7), pp. 505–516.

[7] Lee, S. E., Lee, S.-W., Fischer, P. F., Bassiouny, H. S., and Loth, F., 2008, "Direct Numerical Simulation of Transitional Flow in a Stenosed Carotid Bifurcation," J. Biomech., **41**(11), pp. 2551–2561.

[8] Naghavi, M., Abajobir, A., and Abbafati, C., 2017, "Global, Regional, and National Age-Sex Specifc Mortality for 264 Causes of Death, 1980-2016: A Systematic Analysis for the Global Burden of Disease Study 2016," Lancet, **390**(10100), pp. 1151–1210.

[9] McColgan, P., Bentley, P., McCarron, M., and Sharma, P., 2012, "Evaluation of the Clinical Utility of a Carotid Bruit," QJM, **105**(12), pp. 1171–1177.

[10] Banks, H. T., Hu, S., Kenz, Z. R., Kruse, C., Shaw, S., Whiteman, J. R., Brewin, M. P., Greenwald, S. E., and Birch, M. J., 2014, "Model Validation for a Noninvasive Arterial Stenosis Detection Problem," Math. Biosci. Eng., **11**(3), pp. 427–448.

[11] Varghese, S. S., and Frankel, S. H., 2003, "Numerical Modeling of Pulsatile Turbulent Flow in Stenotic Vessels," ASME J. Biomech. Eng., **125**(4), pp. 445–460.

[12] Steinman, D. A., Poepping, T. L., Tambasco, M., Rankin, R. N., and Holdsworth, D. W., 2000, "Flow Patterns at the Stenosed Carotid Bifurcation: Effect of Concentric Versus Eccentric Stenosis," Ann. Biomed. Eng., **28**(4), pp. 415–423.

[13] Ahmed, S. A., and Giddens, D. P., 1984, "Pulsatile Poststenotic Flow Studies With Laser Doppler Anenometry," J. Biomech., **17**(9), pp. 695–705.

[14] Zarins, C. K., Giddens, D. P., Bharadvaj, B. K., Sottiurai, V. S., Mabon, R. F., and Glagov, S., 1983, "Carotid Bifurcation Atherosclerosis: Quantative Correlation of Plaque Localization With Flow Velocity Profiles and Wall Shear Stress," Circ. Res., **53**(4), pp. 502–514.

[15] Li, Y., Zhu, J., Duperron, M., O'Brien, P., Schüler, R., Aasmul, S., de Melis, M., Kersemans, M., and Baets, R., 2018, "Six-Beam Homodyne Laser Doppler Vibrometry Based on Silicon Photonics Technology," Opt. Express, **26**(3), p. 3638.

[16] Mancini, V., Tommasin, D., Li, Y., Reeves, J., Baets, R., Greenwald, S., and Segers, P., 2019, "Detecting Carotid Stenosis From Skin Vibrations Using Laser Doppler Vibrometry—An In-Vitro Proof-of-Concept," PLoS One, **14**(6), p. e0218317.

[17] Steinman, D. A., 2002, "Image-Based Computational Fluid Dynamics Modeling in Realistic Arterial Geometries," Ann. Biomed. Eng., **30**(4), pp. 483–497.

[18] Mancini, V., Bergersen, A. W., Vierendeels, J., Segers, P., and Valen-Sendstad, K., 2019, "High-Frequency Fluctuations in Post-Stenotic Patient Specific Carotid Stenosis Fluid Dynamics: A Computational Fluid Dynamics Strategy Study," Cardiovasc. Eng. Technol., **10**(2), pp. 277–298.

[19] Iannaccone, F., De Bock, S., De Beule, M., Vermassen, F., Van Herzeele, I., Verdonck, P., Segers, P., and Verhegghe, B., 2014, "Feasibility of a Priori Numerical Assessment of Plaque Scaffolding After Carotid Artery Stenting in Clinical Routine: Proof of Concept," Int. J. Artif. Organs, **37**(12), pp. 928–939.

[20] Kjeldsberg, H. A., Bergersen, A. W., and Valen-Sendstad, K., 2019, "MorphMan: Automated Manipulation of Vascular Geometries," J. Open Source Software, **4**(35), p. 1065.

[21] Antiga, L., Ene-Iordache, B., Caverni, L., Cornalba, G. P., and Remuzzi, A., 2002, "Geometric Reconstruction for Computational Mesh Generation of Arterial Bifurcations From CT Angiography," Comput. Med. Imaging Graph., **26**(4), pp. 227–235.

[22] Vierendeels, J., Merci, B., and Dick, E., 2001, "Numerical Study of Natural Convective Heat Transfer With Large Temperature Differences," Int. J. Numer. Methods Heat Fluid Flow, **11**(4), pp. 329–341.

[23] Likittanasombut, P., Reynolds, P., Meads, D., and Tegeler, C., 2006, "Volume Flow Rate of Common Carotid Artery Measured by Doppler Method and Color Velocity Imaging Quantification (CVI-Q)," J. Neuroimaging, **16**(1), pp. 34–38.

[24] Groen, H. C., Simons, L., van den Bouwhuijsen, Q. J. A., Bosboom, E. M. H., Gijsen, F. J. H., van der Giessen, A. G., van de Vosse, F. N., Hofman, A., van der Steen, A. F. W., Witteman, J. C. M., van der Lugt, A., and Wentzel, J. J., 2010, "MRI-Based Quantification of Outflow Boundary Conditions for

Computational Fluid Dynamics of Stenosed Human Carotid Arteries," J. Biomech., **43**(12), pp. 2332–2338.
[25] Hoi, Y., Wasserman, B. A., Xie, Y. J., Najjar, S. S., Ferruci, L., Lakatta, E. G., Gerstenblith, G., and Steinman, D. A., 2010, "Characterization of Volumetric Flow Rate Waveforms at the Carotid Bifurcations of Older Adults," Physiol. Meas., **31**(3), pp. 291–302.
[26] Ratanakorn, D., and Keandaoungchan, J., 2012, "Volume Flow Rate," Perspect. Med., **1–12**(1), pp. 203–206.
[27] Conti, M., Long, C., Marconi, M., Berchiolli, R., Bazilevs, Y., and Reali, A., 2016, "Carotid Artery Hemodynamics Before and After Stenting: A Patient Specific CFD Study," Comput. Fluids, **141**, pp. 62–74.
[28] Khan, M. O., Steinman, D. A., and Valen-Sendstad, K., 2017, "Non-Newtonian Versus Numerical Rheology: Practical Impact of Shear-Thinning on the Prediction of Stable and Unstable Flows in Intracranial Aneurysms," Int. J. Numer. Method. Biomed. Eng., **33**(7), pp. 1–10.
[29] Khan, M. O., Valen-Sendstad, K., and Steinman, D. A., 2019, "Direct Numerical Simulation of Laminar-Turbulent Transition in a Non-Axisymmetric Stenosis Model for Newtonian vs. Shear-Thinning Non-Newtonian Rheologies," Flow, Turbul. Combust., **102**, pp. 43–72.
[30] Mortensen, M., and Valen-Sendstad, K., 2015, "Oasis: A High-Level/High-Performance Open Source Navier-Stokes Solver," Comput. Phys. Commun., **188**, pp. 177–188.
[31] Khan, M. O., Chnafa, C., Gallo, D., Molinari, F., Morbiducci, U., Steinman, D. A., and Valen-Sendstad, K., 2017, "On the Quantification and Visualization of Transient Periodic Instabilities in Pulsatile Flows," J. Biomech., **52**, pp. 179–182.
[32] Hunt, J. C. R., Wray, A. A., and Moin, P., 1989, "Eddies, Streams and Convergence Zones in Turbulent Flows," Center for Turbulence Research Proceeding Summer Program 1988, Vol. 193.
[33] Fawcett, T., 2006, "An Introduction to ROC Analysis," Pattern Recognit. Lett,., **27**(8), pp. 861–874.
[34] Youden, W. J., 1950, "Index for Rating Diagnostic Tests," Cancer, **3**(1), pp. 32–35.
[35] Jia, Q., Liu, H., Li, Y., Wang, X., Jia, J., and Li, Y., 2017, "Combination of Magnetic Resonance Angiography and Computational Fluid Dynamics May Predict the Risk of Stroke in Patients With Asymptomatic Carotid Plaques," Med. Sci. Monit., **23**, pp. 479–488.
[36] Schirmer, C. M., and Malek, A. M., 2012, "Computational Fluid Dynamic Characterization of Carotid Bifurcation Stenosis in Patient-Based Geometries," Brain Behav., **2**(1), pp. 42–52.
[37] Lee, S.-W., and Steinman, D. A., 2007, "On the Relative Importance of Rheology for Image-Based CFD Models of the Carotid Bifurcation," ASME J. Biomech. Eng., **129**(2), pp. 273–278.
[38] Johansson, E. P., and Wester, P., 2008, "Carotid Bruits as Predictor for Carotid Stenoses Detected by Ultrasonography: An Observational Study," BMC Neurol., **8**(1), pp. 1–8.
[39] Naylor, T. H., and Finger, J. M., 1967, "Verification of Computer Simulation Models," Manage. Sci., **14**(2), pp. 92–106.
[40] Oberkampf, W. L., and Roy, C. J., 2010, *Verification and Validation in Scientific Computing*, Cambridge Press, Cambridge, UK.
[41] Hariharan, P., 2009, "Computational Fluid Dynamics Round Robin Study. Benchmark 1," National Cancer Institute, Bethesda, MD, accessed Mar. 12, 2020, https://fdacfd.nci.nih.gov
[42] Zmijanovic, V., Mendez, S., Moureau, V., and Nicoud, F., 2017, "About the Numerical Robustness of Biomedical Benchmark Cases: Interlaboratory FDA's Idealized Medical Device," Int. J. Numer. Method Biomed. Eng., **33**(1), pp. 1–17.
[43] Bergersen, A. W., Mortensen, M., and Valen-Sendstad, K., 2019, "The FDA Nozzle Benchmark: 'in Theory There is No Difference Between Theory and Practice, but in Practice There Is," Int. J. Numer. Method. Biomed. Eng., **35**(1), p. e3150.
[44] Mancini, V., Tommasin, D., Li, Y., Reeves, J. W., Beats, R., Greenwald, S. E., and Segers, P., 2019, Figshare Dataset of "Detecting Carotid Stenosis From Skin Vibrations Using Laser Doppler Vibrometry—An In Vitro Proof-of-Concept," FigShare.